Influence of oxygen co-implantation on germanium out-diffusion and nanoclustering in SiO2/Si films

Nelis, Adrien; Haye, Emile; Terwagne, Guy

Published in:
Thin Solid Films

DOI:
10.1016/j.tsf.2022.139135

Publication date:
2022

Document Version
Publisher's PDF, also known as Version of record

Thin Solid Films 746 (2022) 139135

Contents lists available at ScienceDirect

Thin Solid Films

journal homepage: www.elsevier.com/locate/tsf

Influence of oxygen co-implantation on germanium out-diffusion and nanoclustering in SiO_2/Si films

A. Nélis *, E. Haye, G. Terwagne

LARN, Namur Institute of Structured Matter (NISM), University of Namur (UNAMUR), B-5000 Namur, Belgium

ARTICLE INFO

Keywords:
Rutherford backscattering spectroscopy
X-ray photoelectron spectroscopy
Germanium
Germanium oxide
Diffusion
Nanocrystals
Ion implantation

ABSTRACT

The thermally activated diffusion of germanium atoms implanted in the middle of SiO_2 layers has been studied by Rutherford Backscattering Spectroscopy (RBS), X-ray Photoelectron Spectroscopy (XPS), μ-Raman spectroscopy and X-Ray Diffraction (XRD), with and without the presence of co-implanted $^{16}O^-$ ions. The important role of implantation-induced defects, in particular atomic recoil of silicon and oxygen atoms, on the well-known asymmetric redistribution of germanium depth-profile is discussed for samples solely implanted with germanium, as a function of the fluence. This is shown how both the stoichiometric state of the implanted SiO_2 layer and their chemical environment influence the mobility of Ge atoms. For samples co-implanted with oxygen, RBS shows an enhancement of germanium diffusion under thermal activation at 1100 °C as long as the oxygen oversaturation of the SiO_2 film is not achieved. This change in the germanium diffusion is associated to the formation of GeO_x compounds during the implantation, as shown by XPS measurements. This is responsible, during the annealing step, of the formation of highly mobile GeO at low oxygen fluences and less mobile GeO_2 at higher fluences. Combination of XRD and μ-Raman analyses is used to highlight the impact of the co-implanted O atoms on the size dispersion of germanium nanocrystals.

1. Introduction

Original approaches are proposed since decades to improve the efficiency of optoelectronic devices [1,2], among which the integration of germanium and silicon nanocrystals in the miniaturization process of such devices [3–7]. Group IV semiconductor nanocrystals open new possibilities thanks to many associated optoelectronic properties. Their tunable bandgap and the potential activation of multiple exciton generation can greatly improve energy conversion in photovoltaic cells. This enhanced photovoltaic efficiency strongly depends on the nanocrystals size and their depth-distribution inside the dielectric layer [4,5,8,9].

In this context, germanium is considered as being a better candidate than silicon for the fabrication of third generation photovoltaic cells thanks to a higher charge carriers mobility, a lower energy bandgap (0.66 eV for Ge versus 1.12 eV for Si) and a large absorption in the visible range.

Ge nanocrystals (Ge-ncs) can be synthesized by ion implantation, which has the advantage of being a technique widely used in silicon-based industry, followed by high temperature treatments (> 800 °C). It has been shown that the nanostructures size and depth-distribution strongly depend on implantation and annealing conditions [9–14].

This post-implantation annealing is known to be responsible of a long-range germanium diffusion leading to an asymmetric redistribution of the germanium depth-profile. This redistribution is associated to the formation of highly mobile GeO and specific irradiation-induced damage occurring during the implantation process [9,11,15,16,17].

In the present work, Rutherford Backscattering Spectroscopy (RBS) and X-ray Photoelectron Spectroscopy (XPS) measurements investigate the effects of the implantation step on germanium redistribution. In agreement with literature [9,10,15,18,19], it is shown that Ge diffusion is controlled by the formation of GeO_x compounds and Ge/Si chemical trapping effects. Special attention is given to recoiled silicon and oxygen atoms to explain the asymmetric redistribution of Ge observed by RBS.

As shown in this study, germanium diffusion is related to the formation of GeO_x compounds and SiO_2 stoichiometry. Its migration can therefore be enhanced by doping, with a co-implantation of oxygen atoms, the under-stoichiometric SiO_x regions where Ge/Si trapping effects generally occur. This leads either to large Ge desorption losses through the gas/SiO_2 interface or germanium oxidation during

* Corresponding author.
E-mail address: adrien.nelis@unamur.be (A. Nélis).

https://doi.org/10.1016/j.tsf.2022.139135
Received 6 July 2021; Received in revised form 23 January 2022; Accepted 7 February 2022
Available online 9 February 2022

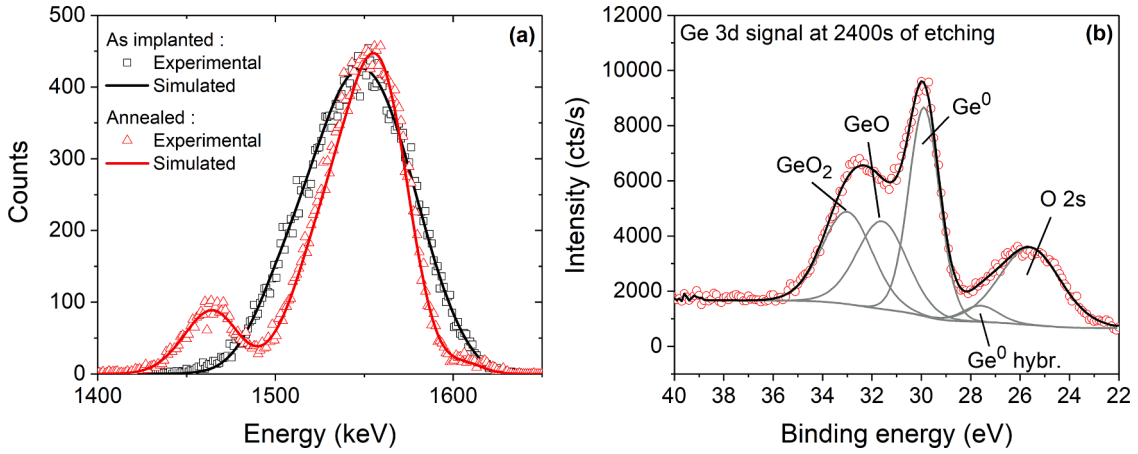

Fig. 1. (a) RBS spectra and fitting curves of a sample implanted with 1.30×10^{17} $^{74}Ge/cm^2$, not co-implanted with oxygen, before (black) and after (red) 60 min of annealing at 1100 °C under N_2. Only the energy range corresponding to germanium signal is shown. (b) Example of XPS fit for the Ge 3d signal for an etching time of 2400 s for the same sample (1.30×10^{17} $^{74}Ge/cm^2$ - 230 keV) before annealing.

annealing, depending on the oxygen saturation of the SiO_2 layer.

The effect of oxygen co-implantation on the nanocrystals formation is also investigated by combination of μ-Raman and X-Ray Diffraction (XRD) measurements. This is shown that the co-implantation of oxygen could be used to reduce the nanocrystals size discrepancies, generally resulting from irradiation-induced damage in implanted films [9-11,20].

2. Experiment

300 nm thick wet-oxidized (100) silicon wafers were implanted with $^{74}Ge^+$ prior to $^{16}O^-$ ions at energies of 230 and 39 keV respectively. SRIM-TRIM [21] (Stopping and Range of Ions in Matter-TRansport of Ions in Matter) simulations have been used to calculate projected ranges, which correspond to 156 nm for $^{74}Ge^+$ and 100 nm for $^{16}O^-$ ions. A germanium fluence ranging from 0.37 to 1.30×10^{17} Ge/cm^2 is used, corresponding to a measured concentration varying from 4.5 to 16 at.% at maximum. The fluence of co-implanted oxygen varies from 0 to 1.66×10^{17} O/cm^2. All implantations were performed with ALTAÏS (Accelerateur Linéaire Tandetron pour l'Analyse et l'Implantation des Solides), the 2 MV Tandetron accelerator installed at LARN (UNamur, Belgium).

A post-implantation annealing was performed for all samples inside a quartz tube furnace heated at 1100 °C for 60 min under N_2, with the facility installed at LARN. A schematic representation of our fabrication process is available in reference [4].

The fluences and depth-profiles of implanted $^{74}Ge^+$ and $^{16}O^-$ ions were verified by RBS, using 2 MeV $^4He^+$ beams for two scattering angles (165 and 135°). RBS data were treated using SIMNRA program [22] in combination with SimTarget (developed by J.L. Colaux [23]).

The chemistry of the samples was investigated by X-ray photoelectron spectroscopy on a Thermo Fisher Escalab 250Xi spectrometer using Al Kα source (1486.68 eV) and a spot size of 250 × 250 μm^2. Samples were profiled using an Ar^+ beam at 1 keV (30°, low current), using a scan mode (pass energy 40 eV, 2 scans) for recording the Ge 3d, Si 2p and O 1s core levels. Fitting is done considering a Shirley background and a Lorentz/Gaussian ratio of 30 and symmetric peak. The authors are aware of the possible damage generation using ion beam, and concentrations obtained are subject to modifications [24,25]. However, ion beam energy has been minimized, and the comparison between samples remains valid, as the same erosion parameters (ion beam energy and current, spot size) have been used.

μ-Raman spectroscopy measurements were carried out using the confocal LabRAM HR800 spectrometer from Horiba Scientific installed at Welcome facility at Université Catholique de Louvain (Belgium). The spectrometer is equipped with a digital camera, a× 100 objective lens and can perform with three different laser wavelengths (488, 514 and 633 nm). The Ar^+ laser probe (λ = 514 nm) was used for all the analyses presented in this study.

The crystallinity of annealed samples and the mean diameter of germanium nanocrystals were measured by XRD measurements with a Cu Kα source (1.5406 Å x-rays, rotating sample), using a panalytical X'Pert PRO Diffractometer in Bragg-Brentano geometry.

3. Results and discussion

3.1. Thermally activated diffusion of Ge

Fig. 1a shows an example of Ge signal measured by RBS, before (black) and after (red) annealing, obtained for a sample solely implanted with a measured fluence of 1.30×10^{17} Ge/cm^2 in the middle of the SiO_2 layer. Only the energy range related to Ge signal is shown. In agreement with previous works in SiO_2/Si films [9,11,13,15,16,20,26,27], an important thermal diffusion of germanium is observed towards both the sample surface (upwards) and the SiO_2/Si interface (downwards). This results in a multi-peak redistribution of the germanium depth-profile, characterized by a highly asymmetric diffusion of implanted Ge atoms.

As already discussed in reference [9], this asymmetric distribution along the sample depth of the germanium profile after annealing results from the combination of three factors: 1) the highly anisotropic composition and crystallography of the implanted medium, 2) the influence of oxygen through the formation of extremely mobile GeO [11,15,18] and 3) the trapping of germanium atoms through the formation of $Ge - Si$ and $Ge - Ge$ chemical bonds [10,19].

The contribution of Ge trapping effects by silicon excess has been presented in reference [9] with the co-implantation of silicon isotopes, while the influence of an atmosphere of annealing contaminated with oxygen has been presented in reference [37] with the use of ^{18}O. The reduction of Ge mobility for increasing Ge fluences is discussed in this work and explained as a function of the stoichiometric state of the SiO_2 film (see Section 3.2).

The example presented in Fig. 1a was chosen because of the Ge/Si trapping effects and oxide damaging which both occur at this fluence during annealing, resulting in the asymmetric diffusion of the implanted Ge atoms. As demonstrated in the next section, at lower fluences Ge diffusion is more efficient and trapping effects are less marked, while the opposite is observed for fluences higher than 1.30×10^{17} Ge/cm^2 [9]. This justifies the use of a fluence of 1.30×10^{17} Ge/cm^2, which allows diffusion and trapping effects to coexist.

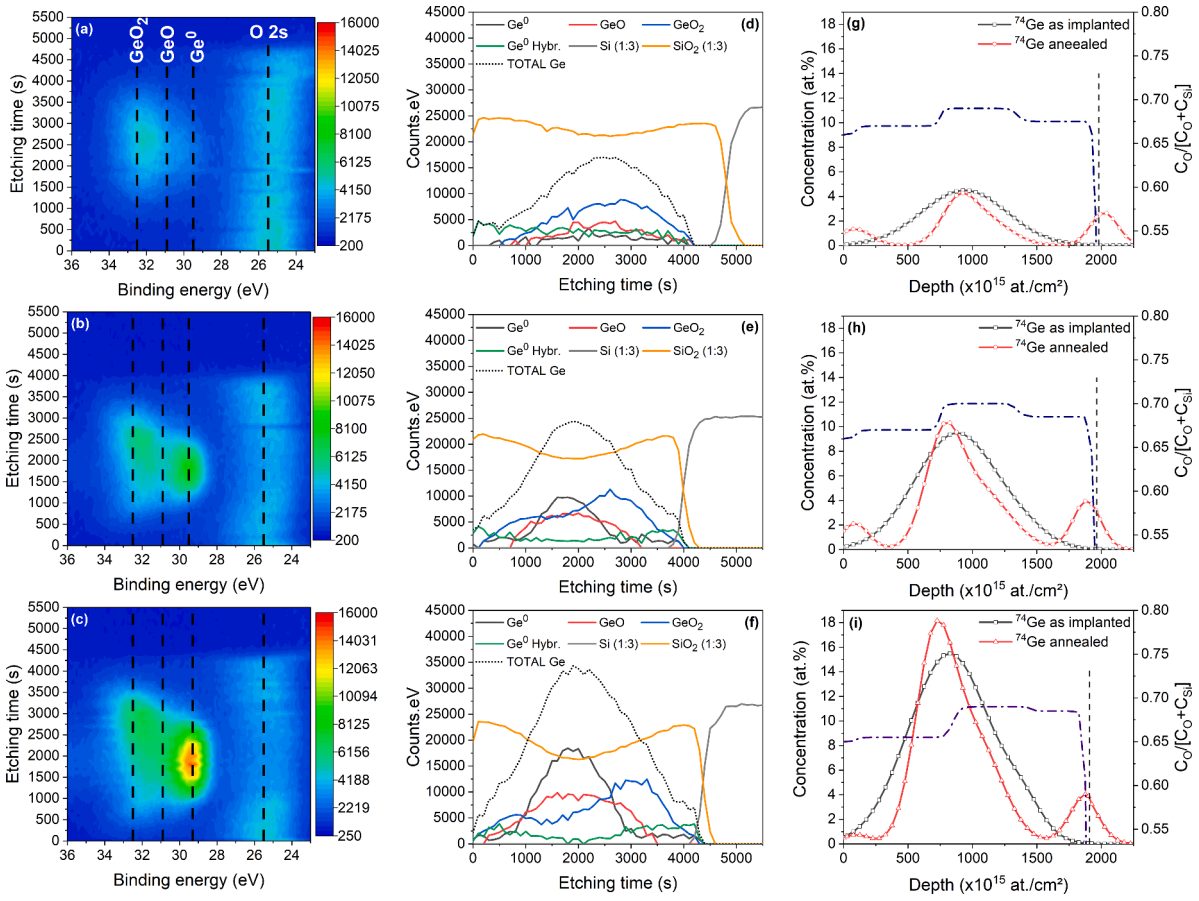

Fig. 2. XPS depth-profiles as a function of etching time before annealing (a-f) and RBS depth-profiles before and after annealing (g-i), for samples solely implanted with germanium with 0.37 $\times 10^{17}$ (a,d,g), 0.80 $\times 10^{17}$ (b,e,h) and 1.30 $\times 10^{17}$ $^{74}Ge/cm^2$ (c,f,i). For better clarity, and due to their strong intensity, Si and SiO_2 signals have been reduced to 1/3 to have representative scale in d-f. $C_O/[C_O + C_{Si}]$ ratio before annealing is plotted by blue broken lines in RBS depth-profiles (right Y-axis).

3.2. *Formation of GeO_x compounds during Ge implantation*

The direct formation of GeO_x compounds during germanium implantations has been observed in SiO_2 layers [15,18,28], but its dependency with germanium fluence is poorly reported in literature, as well as the irradiation-induced changes in the SiO_2 stoichiometry.

Fig. 1b presents a typical fit of the Ge 3d signal, extracted from XPS data, with contributions centered at 29.3, 30.9 and 32.5 eV, corresponding to elemental Ge, GeO, and GeO_2 respectively. The wide peak around 25.5 eV corresponds to O 2s signal. Note that peak position is subject to standard deviation (about 0.3 eV). In some cases, elemental Ge has been observed at binding energies lower than 29.3 eV, probably due to sp^3-like hybridization state resulting in longer chemical bond lengths, and thus lower binding energies [29]. The Si 2p signal has been fitted with two contributions centered at 99.5 and 103.5 eV, corresponding to Si and SiO_2 respectively [30].

Fig. 2a-f present the XPS depth-profiles of unannealed samples solely implanted with germanium for three different fluences, derived from the Ge 3d and Si 2p signals. Fig. 2a-c present a heat map of the Ge 3d signal intensity at different binding energies and as a function of etching time, while Fig. 2d-f present the evolution of the peak area of Ge^0 (black), Ge^0 hybridized (green), GeO (red), GeO_2 (blue), Si (gray) and SiO_2 (yellow) contributions.

XPS data analysis shows that a significant fraction of Ge atoms is present in an oxidized state after the implantation (GeO_x, x being equal to 1 or 2), in the range 30.5 – 33.5 eV. This is consistent with Oswald *et al.* [18] and Beyer *et al.* [15] XPS observations in Ge-implanted SiO_2 layers. These GeO_x compounds formed during the implantation are supposed to be mainly responsible of the long-range diffusion of germanium.

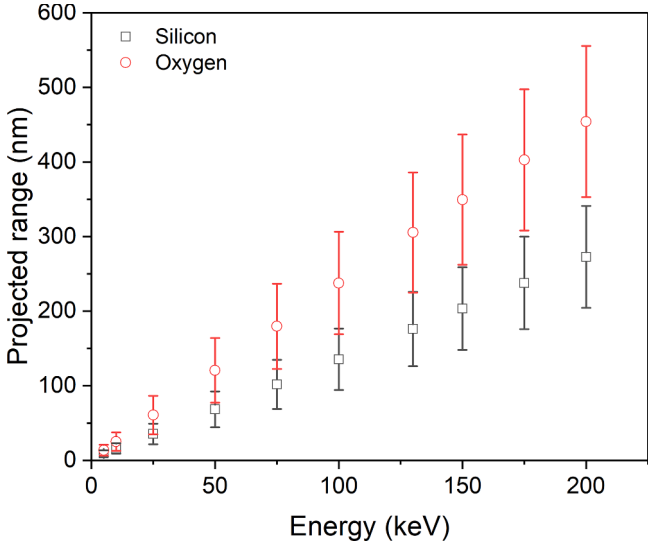

Fig. 3. Results of SRIM-TRIM simulations of projected ranges for Si and O atoms of energy varying from 5 to 200 keV in SiO_2. Error bars represent the longitudinal straggling calculated by SRIM-TRIM.

Along their trajectory through the SiO_2 layer, $^{74}Ge^+$ ions will mainly loss their kinetic energy by Coulomb interactions with Si and O atoms, causing the formation of a large density of recoiled atoms throughout

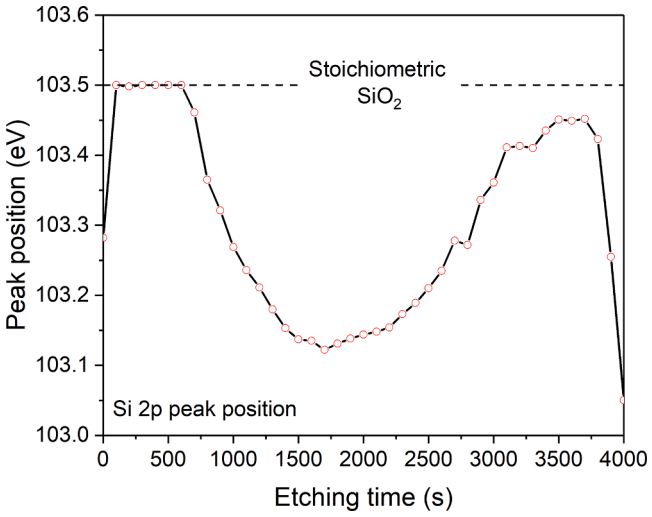

Fig. 4. Evolution of the Si 2p energy shift as a function of the etching time, derived from XPS, for a sample solely implanted with 1.30 × 10^{17} Ge/cm^2 before annealing.

the oxide. According to classical mechanics, the energy transferred to an atom at rest in a single collision is $E = 4m_{ion}m_2E_{ion}\cos^2(\theta)/(m_{ion}+m_2)^2$, where θ is the recoil angle, m_2 is the mass of the target atom, E_{ion} and m_{ion} are the ion energy and mass. According to this, the maximum energy of recoiled Si and O atoms, involved in the particular case of a head-on collision with 230 keV $^{74}Ge^+$ ions, is around 183 and 135 keV respectively. The projected range of these particles, as calculated by SRIM-TRIM, is ~1.3 times greater for oxygen than silicon atoms. In a more general case and at equivalent energy, the oxygen average projected range is 1.68 times higher than that of silicon over an energy range of 5 – 200 keV (Fig. 3). According to the longer projected range of oxygen, in addition to displacement energies two times lower for O than Si (9.3 vs 18.6 eV) [31], the density of Si dangling bonds or Si interstitials will be higher in the region before the maximum of Ge depth-distribution, while recoiled O atoms will concentrate behind the germanium projcted range. This structural reorganization of the oxide leads to the formation of a non-uniform SiO_2 layer with high local stoichiometric discrepancies. This is shown in Fig. 2g-i by blue broken lines, extracted from RBS analyses and representing the concentration ratio $C_O/[C_O + C_{Si}]$. This ratio is equal to ~0.67 for a stoichiometric oxide. Therefore, RBS confirms the formation of an under-stoichiometric oxide (SiO_x, $x < 2$) in the first half of the layer and an over-stoichiometric oxide (SiO_x, $x > 2$) in the second half. This experimental result is in agreement with Beyer and von Borany Tridyn simulations of recoiled O atoms [15]. This also agrees with the XPS observations presented in this study, which systematically exhibit a shift in the positions of O 2s (see Fig. 2a-c and 6a), O 1s and Si 2p peaks (see Fig. 4 for an example of Si 2p energy shift), indicating the formation of non-stoichiometric SiO_x. This chemical environment influences the chemical bonds that implanted Ge atoms will be able to form during both the implantation and the annealing steps, and thus their diffusivity, as the mobility of Ge atoms is lower in SiO_2 films presenting an excess of Si compared to a stoichiometric oxide or a high concentration of Si dangling bonds [9,10,19,26].

XPS depth-profiles (Fig. 2a-f) confirm that GeO_x compounds are formed throughout the entire SiO_2 film, with a concentration which increases as a function of the etching time (up to 3500 s for the highest fluence). This is shown that, as the Ge fluence increases, GeO_2 dominates principally just after the projected range of germanium, while Ge^0 signature becomes dominant in the first part of the Ge depth-profile (between 1000 and 2250 s of etching for the higher Ge fluence), in agreement with the behavior of recoiled Si and O atoms previously highlighted by RBS.

As XPS cannot discriminate Ge-Ge and Ge-Si chemical bonds, due to similar binding energies, Ge^0 contains both contributions. Therefore, Ge^0 signal corresponds to the supposed accumulation of recoiled Si (Ge-Si bonds) and overlaps with the maximum of germanium depth-distribution (Ge-Ge bonds). As reported in literature [11,13,16,19], this Ge^0 region will be the center of Ge nucleation.

Fig. 5 presents the integrated signals of GeO_2, GeO, Ge^0 and Ge^0

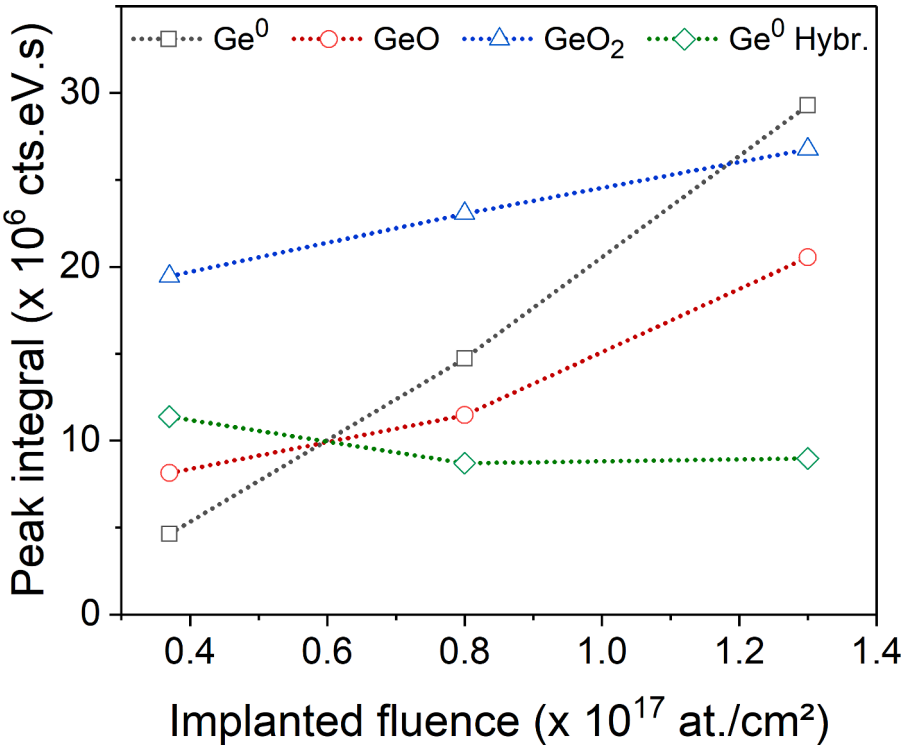

Fig. 5. Evolution of Ge^0, Ge^0 hybr., GeO_2 and GeO integrals measured by XPS as a function of co-implanted fluence. Dotted lines are only there to guide the eye.

Table 1
Distribution of germanium after annealing, as measured by RBS, for samples presented in Fig. 2.

Implanted fluence ($\times 10^{17}$ Ge/cm^2)	Surface peak (%)	Central peak (%)	Interface peak (%)	Losses (%)
0.37	**8.5** ±0.2	**56.0** ±1.1	**21.5** ±0.4	**14.0** ±0.3
0.80	**6.0** ±0.1	**69.0** ±1.4	**15.0** ±0.3	**10.0** ±0.2
1.30	**1.5** ±0.1	**80.0** ±1.6	**11.0** ±0.2	**7.5** ±0.2

hybr.; a direct correlation with the implanted fluence is observed. It can be inferred from Fig. 5 that the fractions of germanium in an oxidized state and Ge^0 are proportional to the implanted fluence, within the range used in this work. GeO_x compounds dominate at low Ge fluences, while Ge^0 concentration increases faster with the Ge fluence. As GeO is highly mobile and germanium poorly mobile when chemically bonded to Ge or Si atoms (both included in Ge^0), this explains the higher germanium mobility observed by RBS for lower Ge fluences, characterized by an

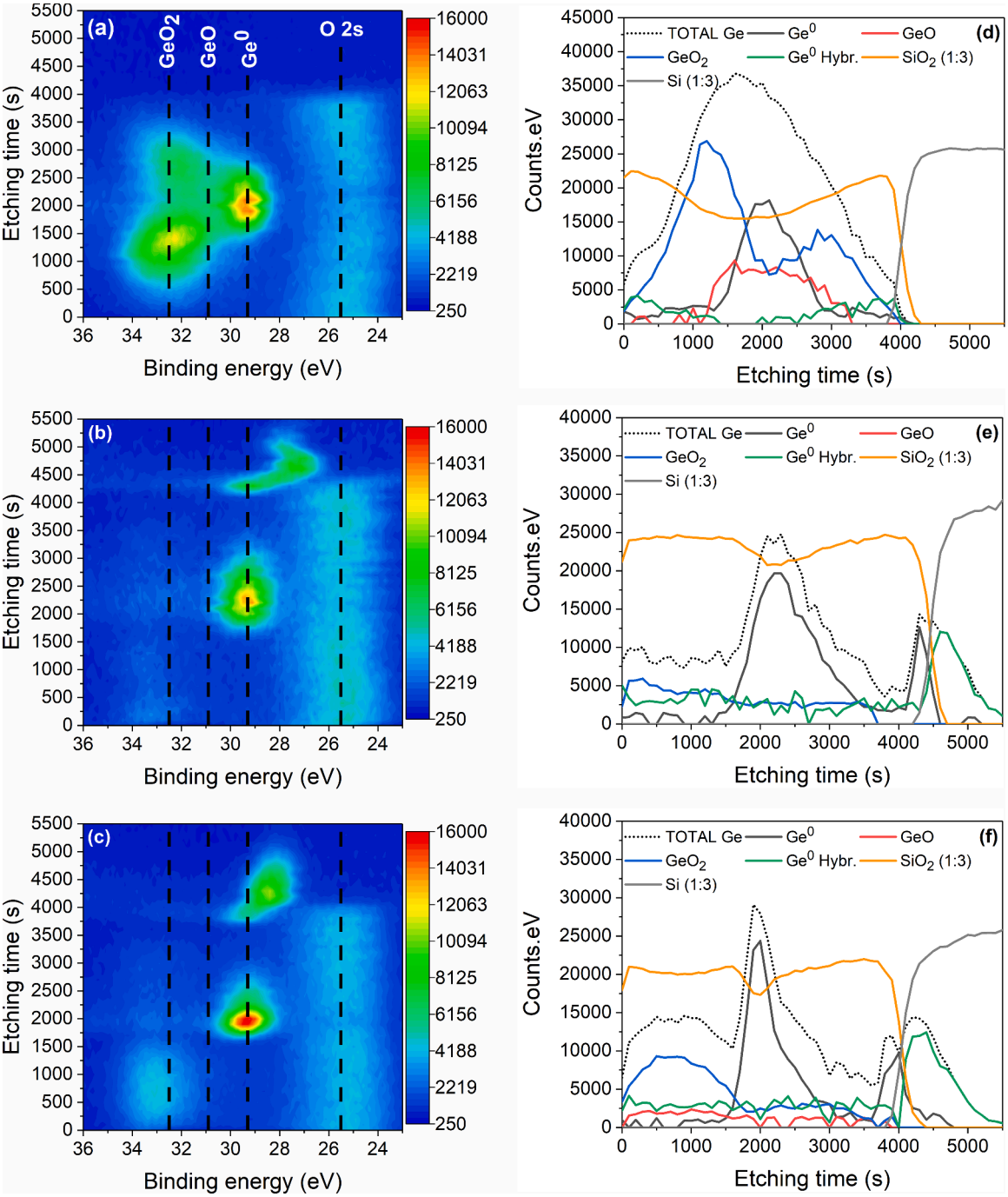

Fig. 6. XPS depth-profiles as a function of etching time for samples co-implanted with 1.30×10^{17} ^{74}Ge/cm^2 and (a) 1.30×10^{17} O$^-$/cm^2 before annealing, (b) 6.9×10^{16} O$^-$/cm^2 after annealing and (c) 1.30×10^{17} O$^-$/cm^2 after annealing. For better clarity, and due to their strong intensity, Si and SiO_2 signals have been reduced to 1/3 to have representative scale.

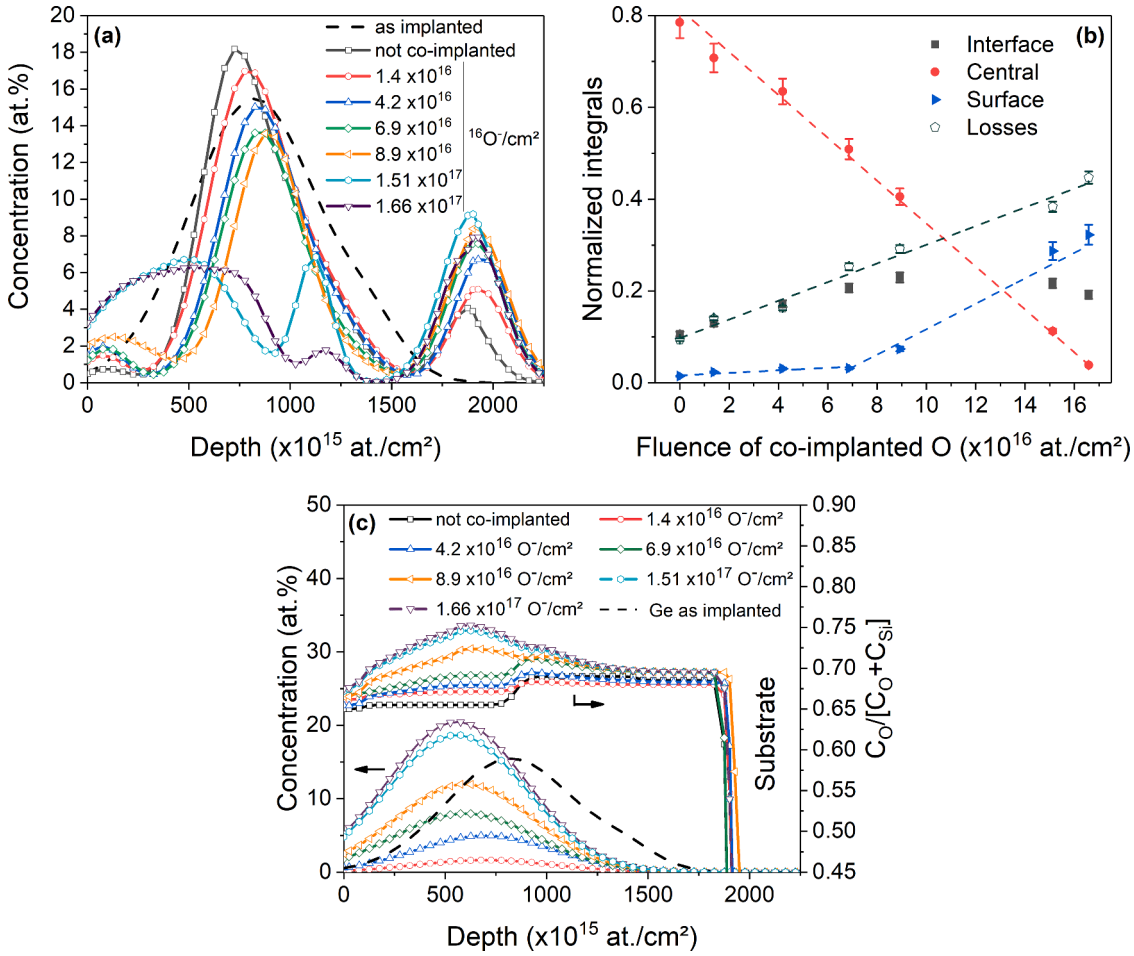

Fig. 7. (a) Superposition of Ge depth-profiles measured by RBS after 60 min of annealing at 1100 °C (N_2) for a fluence of co-implanted oxygen ranging from 0 to 1.66 × 10^{17} O^-/cm^2. (b) Normalized integrals of Ge peaks measured by RBS. (c) Oxygen depth-profiles extracted from RBS analysis (left Y-axis) and $C_O/[C_O+C_{Si}]$ ratio (right Y-axis) before annealing. Oxide saturation is observed when the concentration ratio exceeds the ratio of a stoichiometric oxide (~0.67). The Ge depth-profile of the not co-implanted sample is shown to visualize the overlapping of O and Ge depth-profiles.

enhanced out-diffusion and a more efficient multi-peak redistribution. Added to the large stoichiometric discrepancies measured throughout the oxide layer, and the different Ge diffusivities associated to these regions of the SiO_2 film, this results in the asymmetric redistribution of Ge observed by RBS. This is visible in Ge depth-profiles after annealing (red curves of Fig. 2g-i), and in Table 1 which summarizes the contributions of the three peaks observed by RBS after annealing. The decrease of the amount of Ge within the surface and interface peaks confirms the reduction of the long-range redistribution of Ge as the implantation fluence increases. Note that losses, measured by RBS, stay relatively high (7.5%) for the higher fluence due to the increase of Ge concentration at the extreme surface because of sputtering occurring during the implantation. Near-surface GeO molecules are highly volatile and therefore easily subject to desorption through the sample surface [15].

3.3. Enhanced Ge diffusion by co-implantation of oxygen

To improve germanium diffusion during annealing, a co-implantation of $^{16}O^-$ ions has been inserted between Ge implantation and annealing steps. As the implantation energy of the oxygen ions is 39 keV, the oxygen depth-profile is distributed at around 100 nm from the sample surface, i.e. in the oxide region most subject to irradiation-induced damaging. Co-implanted oxygen atoms will have three effects: 1) enhancing the Ge diffusion through the formation of GeO molecules [15,18], 2) regenerating the stoichiometry of the damaged SiO_2 layer by oxidizing the Si dangling bonds and Si interstitials [15], or 3) oxidizing Ge when SiO_2 saturation is achieved.

The XPS depth-profile (Fig. 6a and d) of a co-implanted sample, without annealing, shows that co-implanted oxygen chemically binds to germanium to form GeO_2 at a depth where their concentration profiles overlap, namely at etching time of 0 – 2500 s. XPS results indicate that GeO_2 depth-distribution exhibits a maximum for an etching time of 1300 s, which corresponds to the first third of the SiO_2 layer measured by XPS. This value is consistent with the projected range of $^{16}O^-$ ions calculated by SRIM-TRIM simulation (100 nm).

Seven samples have been co-implanted with fluences ranging from 0 to 1.66 × 10^{17} O/cm^2, for a single Ge fluence of 1.30 × 10^{17} Ge/cm^2. This range of fluences allows a constant evolution of the relative concentration of implanted oxygen atoms compared to Ge, until the concentration at maximum of added O atoms exceeds that of Ge (Fig. 7c). To simplify the discussion, Ge depth-distributions of annealed samples are superimposed in Fig. 7a and normalized integrals are shown in Fig. 7b. The depth-profiles of oxygen, derived from RBS measurements before annealing, are shown in Fig. 7c, as well as the $C_O/[C_O+C_{Si}]$ concentration ratio. Several effects on the multi-peak redistribution of Ge, attributed to oxygen co-implantation, are highlighted by RBS (Fig. 7) and XPS (Fig. 6) data analysis after thermal treatment:

1) According to XPS, the central peak is mainly composed of elemental Ge after annealing. As oxidized Ge compounds are thermodynamically less stable than oxidized Si at high temperature [32,33], the

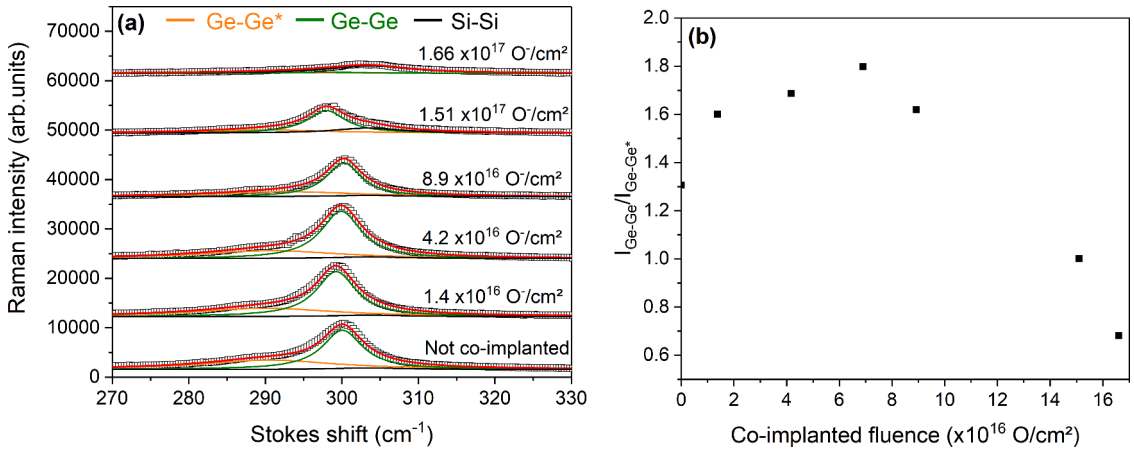

Fig. 8. (a) μ-Raman measurements focused on frequencies corresponding to Ge nanocrystals signal, and (b) evolution of I_{Ge-Ge}/I_{Ge-Ge^*} ratio as a function of co-implanted oxygen fluence.

following oxygen exchange is expected to occur during annealing until the SiO_2 stoichiometry is restored:

$$GeO_x + SiO_x \rightarrow Ge + SiO_2, \quad (1)$$

$$GeO_x + Si \rightarrow Ge + SiO_x. \quad (2)$$

This tendency of the SiO_2 layer to recover its stoichiometry is confirmed by XPS for annealed samples (Fig. 6), which shows that the SiO_2 stoichiometry is globally restored after annealing, as O 2s signal is no longer shifted. The central peak integral, measured by RBS, decreases by 95% while O fluence increases from 0 to 1.66 × 10^{17} O/cm^2 (Fig. 7b). This diminution seems to be proportional to the co-implanted fluence over the full range. For low O fluences, additional oxygen will bind with both Si and Ge atoms to form SiO_x and GeO_x compounds during the implantation. During annealing, the SiO_x concentration decreases as the SiO_2 stoichiometry is restored (Eq. (1)), leading to a lower density of Si dangling bonds. At the same time, mobile GeO molecules are formed rather than GeO_2, as long as the oxygen excess stays relatively low compared to the Ge concentration, due to the following reaction [34,35]:

$$GeO_2 + Ge \rightarrow 2GeO. \quad (3)$$

Therefore, mobile GeO can diffuse easier as the Ge/Si trapping effects [9,10] due to silicon dangling bonds are reduced in this region of the oxide, from 0 to 1000 × 10^{15} at./cm^2, for samples co-implanted with oxygen. These mobile GeO molecules, generally considered as the main responsible of the Ge redistribution, can diffuse from the central peak towards oxygen-poor regions such as the SiO_2/Si interface or the sample surface. This is confirmed by RBS with the increase in Ge concentration in these two regions of the SiO_2 layer, accompanied by a reduction in Ge concentration in the central peak, as the O fluence increases (Fig. 7b).

2) A sub-surface peak of fully oxidized germanium (GeO_2) appears after annealing when the oxygen fluence increases, as indicated in Fig. 6. For low oxygen concentrations, this peak is supposed to be due to additional oxygen in the damaged layer, leading to the formation of GeO molecules, and to the presence of residual impurities (H_2O, O_2) in the annealing environment [11,13,16,36,37]. The encounter of out-diffusing GeO with in-diffusing O_2 coming from the annealing atmosphere forces the oxidation of Ge. For higher oxygen fluences, the concentration of oxygen is so high that the SiO_2 oxide is saturated, as shown in Fig. 7c by the $C_O/[C_O + C_{Si}]$ concentration ratios. The saturation is observed when the concentration ratio exceeds the ratio of a stoichiometric oxide (~0.67). The exceeding oxygen is therefore available to oxidize germanium atoms or GeO molecules to form GeO_2, if the concentration of O atoms is at least comparable to that of Ge atoms (to avoid reaction 3). The mobility of fully oxidized germanium is highly reduced compared to that of GeO.

   XPS data confirm that GeO_2 formation occurs already during the implantation of oxygen (Fig. 6d) and that this sub-surface peak is composed of GeO_2 after the annealing step (Fig. 6f). The formation of this few mobile GeO_2 explains the extension of the sub-surface peak observed for higher oxygen fluences in both RBS and XPS measurements.

3) The integral of the SiO_2/Si interface peak increases with the oxygen fluence before saturating for higher fluences (black squares in Fig. 7b). This indicates that the fraction of GeO diffusing in depth also increases with the co-implanted O fluence. This can be attributed to an increase of oxygen concentration, and so GeO concentration, with the oxygen fluence Fig. 7c), and to the over-stoichiometric state of the oxide between the Ge projected range and the SiO_2/Si interface which promotes diffusion. This demonstrates that GeO also diffuses towards the oxygen-poor regions such as the SiO_2/Si interface, which is known to be under-stoichiometric [38], where it reduces in elemental Ge (Eqs. (1)-(2). XPS measurement on annealed samples (Fig. 6b, c, e, f) confirms that this interface peak is composed of Ge-Ge and Ge-Si bonds (Ge^0 and Ge^0 hybr.). However, if Baranwal *et al.* has observed the presence of Ge nanocrystals in the vicinity of the interface [20], using transmission electron microscopy (TEM) investigations, it was evidenced by Markvitz *et al.* that the formation of such bonds would not necessarily lead to the nucleation of Ge [11]. Nevertheless, note that one could imagine to use this accumulation of Ge at the SiO_2/Si interface to reduce the current crowding effects occurring in MOS gate-controlled device structures [39].

4) Fig. 7b shows an increase of 450% of desorption losses through the sample surface observed for co-implantation fluences varying from 0 to 1.66 × 10^{17} O/cm^2. As already discussed, the presence of additional oxygen atoms saturates the Si dangling bonds and therefore reduces the Ge/Si trapping effects [9,10,26]. This also leads to the formation of mobile GeO, giving rise to a diffusion directed towards the oxygen-poor regions, such as the sample surface. There, the highly volatile GeO molecules desorb through the surface. These losses increase with the concentration of GeO present in the sample and specially in the vicinity of the sample surface in co-implanted samples.

3.4. Influence on Ge nanoclustering

μ-Raman and XRD analyses were performed to highlight the impact

Table 2
Evolution of nanocrystals average size as measured by XRD and calculated using Scherrer's equation.

Co-implanted fluence ($\times 10^{17}$ O/cm^2)	0	0.14	0.42	0.69	0.89
Mean diameter (nm)	**7.0** ±0.3	**7.2** ±0.4	**7.8** ±0.4	**8.5** ±0.4	**8.2** ±0.7

of oxygen co-implantation over Ge nanoclustering. μ-Raman spectra are shown in Fig. 8a within the spectral range of 270 - 330 cm^{-1}, chosen to eliminate the strong contribution of the TO phonon mode of the Si substrate around 520.7 cm^{-1} and to zoom on the region where Raman phonons related to Ge nanocrystals appear [40]. In agreement with previous studies [9,10,40-41] two contributions are observed at about 291 and 300 cm^{-1} in Fig. 8a. These peaks are associated to the signature of small Ge nanocrystals (or containing Si impurities) and pure Ge nanocrystals, respectively.

As previously shown by XPS and RBS analyses, the SiO_2 region mainly impacted by co-implanted oxygen ions (for an etching time of 0 - 2000 s) is the damaged zone of the film which corresponds to the growth region of smaller nanocrystals (or nanocrystals containing Si) [10,20].

The evolution of Raman peaks integrals is shown in Fig. 8b. As absolute intensities are hard to compare in Raman spectroscopy, we use the ratio I_{Ge-Ge}/I_{Ge-Ge^*}, which represents the integrals ratio between pure (Ge-Ge) and Si-contaminated or very small nanocrystals (Ge-Ge*). An increase of this ratio is observed between 0 and 6.9 $\times$ 10^{16} O/cm^2, which indicates that the density of small nanocrystals (Raman peak around 291 cm^{-1}) decreases continuously, compared to that of large and pure Ge-ncs, within this range of oxygen fluences. As the growth region of small nanocrystals coincides with the projected range of co-implanted oxygen ions, this diminution of small nanocrystals signature in Raman spectra is consistent with the increased Ge diffusion highlighted by RBS and XPS measurements in this region for lower oxygen fluences. For higher oxygen concentrations, I_{Ge-Ge}/I_{Ge-Ge^*} ratio decreases with oxygen fluence, meaning a diminution of the density of pure germanium nanocrystals (Raman peak around 300 cm^{-1}), which can be attributed to the too high Ge diffusion, and the subsequent decrease of the Ge content in the central peak, and to the direct formation of amorphous GeO_2, as shown by XPS and RBS (Figs. 6 and 7).

Note that a very weak Raman signal is measured at around 400–405 cm^{-1} from an oxygen fluence of 4.17 $\times$ 10^{16} O/cm^2, with a slight increase in intensity with oxygen fluence. This peak corresponds to Ge-Si chemical bonds and is supposed to be due to the increase of Ge concentration at the SiO_2/Si interface and the subsequent formation of Ge-Si bonds.

The evolution of the nanocrystals mean diameter has been studied by XRD measurements, with analyses focused on Ge (111) signal around 27.4°, for a range of fluences between 0 and 8.9 $\times$ 10^{16} O/cm^2 (corresponding to the range of fluences ensuring a minimum amount of Ge in the central peak). XRD exhibits the same trend that Raman spectra, with a constant diminution of the peak broadening until a fluence of 6.9 $\times$ 10^{16} O/cm^2. This indicates a standardization of nanocrystals size, which could be consistent with an elimination of small nanocrystals and the conservation of larger nanostructures. Using Scherrer's equation and taking into account instrumental broadening, the Ge nanocrystals average size is calculated and reported in Table 2 and Fig. 9. It is shown that the nanocrystals average size increases with the co-implanted fluence, which tends to confirm the disappearance of small nanostructures to the benefit of larger ones, thanks to a slightly enhanced Ge diffusion. For the higher O fluences, the SiO_2 oversaturation and the subsequent poor amount of elemental Ge prevents the formation of Ge-ncs.

These μ-Raman and XRD results indicate that oxygen co-implantation could be used to locally reduce the size dispersion of Ge nanocrystals, an effect which increases with the Ge fluence [12], by preserving only the purest Ge-ncs while removing small nanocrystals. After the possibility of controlling the diffusion of Ge and the size distribution in depth of Ge nanocrystals by Si co-implantation [9,10,19], introduction of oxygen excess could be another tool in a precise control of nanocrystals size dispersion. This study demonstrates that the O fluence must stay relatively low to enhance Ge diffusion while limiting its desorption or the formation of GeO_2. As Ge-ncs photoluminescence (PL) could partially depend of the nanocrystals size and their Si contamination [33,42], an uniform size distribution could reduce the broad PL emission observed for Ge-ncs in SiO_2 [43], making them possibly more suitable for applications such as lasers.

4. Conclusions

Combination of RBS and XPS investigations confirmed the role played by GeO formation and ion damaging, which both occur simultaneously during germanium implantation, on the thermally activated diffusion of Ge atoms implanted in the middle of SiO_2 films. The results highlight the effects of both the Ge fluence and the stoichiometric state of the implanted SiO_2 film on the diffusion of germanium, explaining the large discrepancies observed in literature. It is shown that the concentrations of GeO_x compounds and Ge^0 linearly increase with the

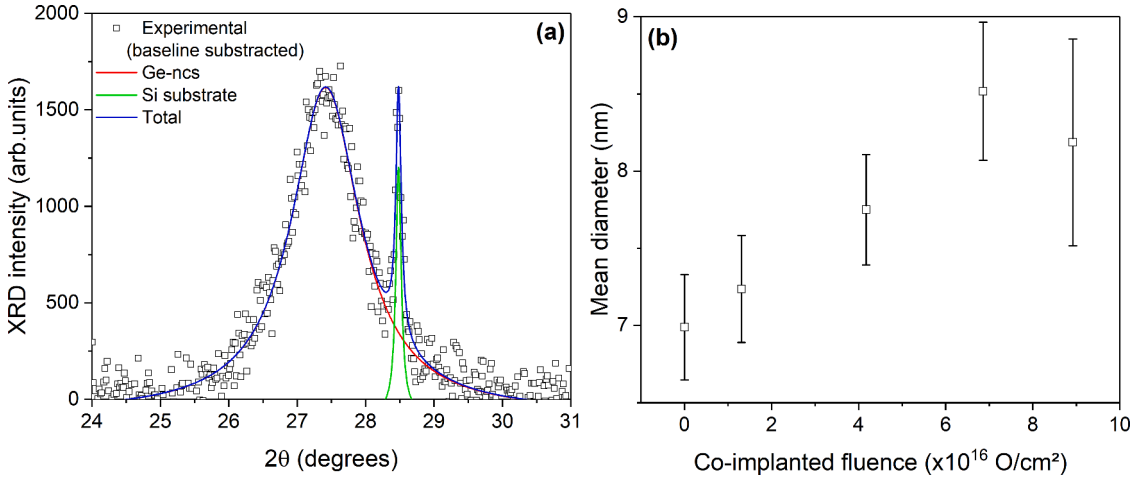

Fig. 9. (a) Example of a fit with Ge nanocrystals peak around 27.4° and Si substrate signal around 28.45° (b) Evolution of nanocrystals mean diameter as a function of the oxygen fluence.

germanium fluence with different slopes, leading to different dominations as a function of the implanted fluence. This explains why germanium diffusion is generally improved in SiO_2 layers implanted with low Ge fluences compared to higher fluences.

As implanted samples are characterized by large discrepancies in the size of the thermally grown nanostructures, due to specific irradiation-induced damage, the use of oxygen co-implantation is suggested to prevent the formation of the smallest nanocrystals. It is shown by RBS and XPS, and supported by μ-Raman and XRD measurements, that the introduction of oxygen excess in the damaged regions of the SiO_2 film can improve the mobility of Ge atoms. At relatively low O concentration, the gain in Ge mobility enables to increase the average size of nanocrystals. At higher O fluences, the high mobility of GeO causes the desorption of germanium through the sample surface until the oversaturation of the oxide, which leads to the formation of fixed GeO_2.

Data availability

The data that support the findings of this study are available from the corresponding author upon request.

CRediT authorship contribution statement

A. Nélis: Conceptualization, Investigation, Formal analysis, Writing – original draft, Writing – review & editing. **E. Haye:** Investigation, Formal analysis, Writing – review & editing. **G. Terwagne:** Supervision, Writing – review & editing.

Declaration of Competing Interest

The authors declare that they have no known competing financial interests or personal relationships that could have appeared to influence the work reported in this paper.

Acknowledgments

The authors would like to thanks Welcome platform for the accessibility to the spectrometer and especially Ferran Urena Begara for his help, T. Tabarrant for the technical support on ALTAÏS accelerator, SIAM (Synthesis, Irradiation and Analysis of Materials) and PC^2 (Physico-Chemical Characterization) technological platforms of the University of Namur for XPS and XRD measurements.

References

[1] K. Xu, L. Huang, Z. Zhang, J. Zhao, Z. Zhang, L.W. Snyman, J.W. Swart, Light emission from a poly-silicon device with carrier injection engineering, Mater. Sci. Eng. 231 (2018) 28–31, https://doi.org/10.1016/j.mseb.2018.07.002.

[2] J. Márquez, H. Stange, C.J. Hages, N. Schaefer, S. Levcenko, S. Giraldo, E. Saucedo, K. Schwarzburg, D. Abou-Ras, A. Redinger, M. Klaus, C. Genzel, T. Unold, R. Mainz, Chemistry and dynamics of Ge in Kesterite: toward band-gap-graded absorbers, Chem. Mater. 29 (21) (2017) 9399–9406, https://doi.org/10.1021/acs.chemmater.7b03416.

[3] M.A. Green, S.P. Bremner, Energy conversion approaches and materials for high-efficiency photovoltaics, Nat. Mater. 16 (2017) 23–34, https://doi.org/10.1038/nmat4676.

[4] M. Yedji, J. Demarche, G. Terwagne, R. Delamare, D. Flandre, D. Barba, D. Koshel, G.G. Ross, Method for fabricating third generation photovoltaic cells based on Si quantum dots using ion implantation into SiO 2, J. Appl. Phys. 109 (8) (2011), 084337, https://doi.org/10.1063/1.3575325.

[5] M.C. Beard, K.P. Knutsen, P. Yu, Q. Song, J. Luther, R. Ellingson, A.J. Nozik, Multiple exciton generation in colloidal silicon nanocrystals, Nano Lett. 7 (2007) 2506–2512, https://doi.org/10.1021/nl071486l.

[6] T. Nann, W.M. Skinner, Quantum dots for electro-optic devices, ACS Nano 5 (7) (2011) 5291–5295, https://doi.org/10.1021/nn2022974.

[7] H.I. Hanafi, S. Tiwari, I. Khan, Fast and long retention-time nano-crystal memory, IEEE Trans. Electron. Device. 43 (1996) 1553–1558, https://doi.org/10.1109/16.535349.

[8] M.T. Trinh, R. Limpens, W.D.A.M. de Boer, J.M. Schins, L.D.A. Siebbeles, T. Gregorkiewicz, Direct generation of multiple excitons in adjacent silicon nanocrystals revealed by induced absorption, Nat. Photon. 6 (5) (2012) 316–321, https://doi.org/10.1038/nphoton.2012.36.

[9] A. Nélis, D. Barba, G. Terwagne, Control of germanium diffusion using low quantities of co-implanted silicon isotopes, J. Appl. Phys. 128 (12) (2020), 125705, https://doi.org/10.1063/5.0020368.

[10] D. Barba, C. Wang, A. Nélis, G. Terwagne, F. Rosei, Blocking germanium diffusion inside silicon dioxide using a co-implanted silicon barrier, J. Appl. Phys. 123 (16) (2018), 161540, https://doi.org/10.1063/1.5002693.

[11] A. Markwitz, B. Schmidt, W. Matz, R. Grötzschel, A. Mücklich, Microstructural investigation of ion beam synthesised germanium nanoclusters embedded in SiO2 layers, Nucl. Instrum. Methods Phys. Res. B 142 (3) (1998) 338–348, https://doi.org/10.1016/S0168-583X(98)00283-3.

[12] L.H. Ge, C. Wang, R.S. Cai, W.S. Liang, Y.Q. Wang, G.G. Ross, D. Barba, Effect of Ge concentration on the microstructure of germanium nanocrystals produced by ion implantation in SiO 2, Nanosci. Nanotechno. 17 (3) (2017) 2196–2200, https://doi.org/10.1166/jnn.2017.12858.

[13] K. Heinig, B. Schmidt, A. Markwitz, R. Grötzschel, M. Strobel, S. Oswald, Precipitation, ripening and chemical effects during annealing of Ge+ implanted SiO2 layers, Nucl. Instrum. Methods Phys. Res. B 148 (1–4) (1999) 969–974, https://doi.org/10.1016/S0168-583X(98)00862-3.

[14] E.S. Marstein, A.E. Gunnæs, U. Serincan, S. Jørgensen, A. Olsen, R. Turan, T. G. Finstad, Mechanisms of void formation in Ge implanted SiO2 films, Nucl. Instrum. Methods Phys. Res. B 207 (4) (2003) 424–433, https://doi.org/10.1016/S0168-583X(03)00965-0.

[15] V. Beyer, J. von Borany, Elemental redistribution and Ge loss during ion-beam synthesis of Ge nanocrystals in SiO2 films, Phys. Rev. B 77 (1) (2008), 014107, https://doi.org/10.1103/PhysRevB.77.014107.

[16] J. von Borany, R. Grötzschel, K.H. Heinig, A. Markwitz, W. Matz, B. Schmidt, W. Skorupa, Multimodal impurity redistribution and nanocluster formation in Ge implanted silicon dioxide films, Appl. Phys. Lett. 71 (22) (1997) 3215–3217, https://doi.org/10.1063/1.120294.

[17] X. Hao, C. Zhou, R. Yu, B. Wang, L. Wei, Characterization of implantation induced defects in Si-implanted SiO 2 film, Nanosci. Nanotechno. 8 (3) (2008) 1350–1354, https://doi.org/10.1166/jnn.2008.327.

[18] S. Oswald, B. Schmidt, K.-.H. Heinig, XPS investigation with factor analysis for the study of Ge clustering in SiO2, Surf. Interface Anal. 29 (4) (2000) 249–254, https://doi.org/10.1002/(SICI)1096-9918(200004)29:4≤249::AID-SIA735≥3.0.CO;2-5.

[19] D. Barba, J. Demarche, F. Martin, G. Terwagne, G.G. Ross, Trapping of diffusing germanium by silicon excess co-implanted into fused silica, Appl. Phys. Lett. 101 (14) (2012), 143107, https://doi.org/10.1063/1.4757291.

[20] V. Baranwal, J.W. Gerlach, A. Lotnyk, B. Rauschenbach, H. Karl, S. Ojha, A. C. Pandey, Embedded Ge nanocrystals in SiO 2 synthesized by ion implantation, J. Appl. Phys. 118 (13) (2015), 134303, https://doi.org/10.1063/1.4932151.

[21] J.F. Ziegler, M.D. Ziegler, J.P. Biersack, SRIM – The stopping and range of ions in matter (2010), Nucl. Instrum. Methods Phys. Res. B 268 (11–12) (2010) 1818–1823, https://doi.org/10.1016/j.nimb.2010.02.091.

[22] M. Mayer, SIMNRA, a simulation program for the analysis of NRA, RBS and ERDA, in: AIP Conf. Proc, 1999.

[23] J.L. Colaux, Characterization of carbon nitride compounds synthesized by simultaneous implantation of carbon and nitrogen in copper. Doctoral Dissertation, University of Namur, 2009.

[24] G. Greczynski, L. Hultman, X-ray photoelectron spectroscopy: towards reliable binding energy referencing, Prog. Mater. Sci. 107 (2020), 100591, https://doi.org/10.1016/j.pmatsci.2019.100591.

[25] L. Rassinfosse, J.L. Colaux, D. Pilloud, A. Nominé, N. Tumanov, S. Lucas, E. Haye, Using ammonia for reactive magnetron sputtering, a possible alternative to HiPIMS? Appl. Phys. Lett. 502 (2020), 144176 https://doi.org/10.1016/j.apsusc.2019.144176.

[26] D. Barba, R.S. Cai, J. Demarche, Y.Q. Wang, G. Terwagne, F. Rosei, G.G. Ross, Influence of silicon dangling bonds on germanium thermal diffusion within SiO 2 glass, Appl. Phys. Lett. 104 (11) (2014), 111901, https://doi.org/10.1063/1.4868721.

[27] A. Rodríguez, T. Rodríguez, Á.C. Prieto, J. Jiménez, A. Kling, C. Ballesteros, J. Sangrador, Crystallization of amorphous Si0.6Ge0.4 nanoparticles embedded in SiO2: crystallinity versus compositional stability, J. Electon. Mater. 39 (8) (2010) 1194–1202, https://doi.org/10.1007/s11664-010-1254-9.

[28] H.B. Kim, K.H. Chae, C.N. Whang, J.Y. Yeong, M.S. Oh, S. Im, J.H. Song, The origin of photoluminescence In Ge-implanted SiO2 layers, J. Lumin. 80 (1998) 281–284, https://doi.org/10.1109/IMNC.1998.730045.

[29] H.-.S. Tsai, Y.-.Z. Chen, H. Medina, T.-.Y. Su, T.-.S. Chou, Y.-.H. Chen, J.-.H. Liang, Direct formation of large-scale multi-layered germanene on Si substrate, Phys. Chem. Chem. Phys. 17 (33) (2015) 21389–21393, https://doi.org/10.1039/C5CP02469B.

[30] D.S. Jensen, S.S. Kanyal, N. Madaan, M.A. Vail, A.E. Dadson, M.H. Engelhard, M. R. Linford, Silicon (100)/SiO 2 by XPS, Surf. Sci. Spectra 20 (1) (2013) 36–42, https://doi.org/10.1116/11.20121101.

[31] R.L. Pfeffer, Damage center formation in SiO2 thin films by fast electron irradiation, J. Appl. Phys. 57 (12) (1985) 5176–5180, https://doi.org/10.1063/1.335252.

[32] K. Prabhakaran, F. Maeda, Y. Watanabe, T. Ogino, Distinctly different thermal decomposition pathways of ultrathin oxide layer on Ge and Si surfaces, Appl. Phys. Lett. 76 (16) (2000) 2244–2246, https://doi.org/10.1063/1.126309.

[33] M.P. Gambaryan, G.K. Krivyakin, S.G. Cherkova, M. Stoffel, H. Rinnert, M. Vergnat, V.A. Volodin, Quantum size effects in germanium nanocrystals and amorphous nanoclusters in GeSixOy films, Phys. Solid State 62 (3) (2020) 492–498, https://doi.org/10.1134/S1063783420030105.

[34] J. Oh, J.C. Campbell, Thermal desorption of Ge native oxides and loss of Ge from the surface, J. Electon. Mater. 33 (4) (2004) 364–367, https://doi.org/10.1016/j.mssp.2010.10.009.
[35] P.-.E. Hellberg, S.-.L. Zhang, F.M. D'Heurle, C.S Petersson, Oxidation of silicon–germanium alloys. II. A mathematical model, J. Appl. Phys. 82 (11) (1997) 5779–5787, https://doi.org/10.1063/1.366444.
[36] V.A. Borodin, K.-.H. Heinig, B. Schmidt, Modeling of Ge nanocluster evolution in ion-implanted SiO2 layer, Nucl. Instrum. Methods Phys. Res. B 147 (1–4) (1999) 286–291, https://doi.org/10.1016/S0168-583X(98)00562-X.
[37] A. Nélis, I. Vickridge, J.-.J. Ganem, E. Briand, G. Terwagne, 18O(p,α) 15 N isotopic tracing of germanium diffusion in SiO2/Si films, J. Appl. Phys. 130 (10) (2021), 105701, https://doi.org/10.1063/5.0057968.
[38] Y. Takakuwa, M. Nihei, N. Miyamoto, Outdiffusion and subsequent desorption of volatile SiO molecules during annealing of thick SiO 2 films in vacuum, Jpn. J. Appl. Phys. 32 (4A) (1993) L480–L483, https://doi.org/10.1143/JJAP.32.L480. Part 2.
[39] K. Xu, Silicon electro-optic micro-modulator fabricated in standard CMOS technology as components for all silicon monolithic integrated optoelectronic systems, J. Micromech. Microeng. 31 (2021), 054001, https://doi.org/10.1088/1361-6439/abf333.
[40] D. Barba, J. Demarche, F. Martin, G. Terwagne, G.G. Ross, Control of the Ge nanocrystal synthesis by co-implantation of Si +, J. Appl. Phys. 114 (7) (2013), 074306 https://doi.org/10.1063/1.4817667.
[41] L.Z. Liu, F. Gao, X.L. Wu, T.H. Li, P.K. Chu, Influence of GeSi interfacial layer on Ge–Ge optical phonon mode in SiO2 films embedded with Ge nanocrystals, Appl. Phys. Lett. 95 (17) (2009), 171105, https://doi.org/10.1063/1.3257379.
[42] S. Takeoka, K. Toshikiyo, M. Fujii, S. Hayashi, K. Yamamoto, Photoluminescence fromSi1-xGex alloy nanocrystals, Phys. Rev. B 61 (23) (2000) 15988–15992, https://doi.org/10.1103/PhysRevB.61.15988.
[43] W.K. Choi, Y.W. Ho, S.P. Ng, V. Ng, Microstructural and photoluminescence studies of germanium nanocrystals in amorphous silicon oxide films, J. Appl. Phys. 89 (4) (2001) 2168–2172, https://doi.org/10.1063/1.1342026.